

Wave-ice interactions in the marginal ice zone. Part 2: Numerical implementation and sensitivity studies along 1D transects of the ocean surface

Timothy D. Williams^a, Luke G. Bennetts^b, Vernon A. Squire^c, Dany
Dumont^d, Laurent Bertino^{a,e}

^a*Nansen Environmental and Remote Sensing Center, Thormøhlensgate 47, 5006 Bergen,
Norway*

^b*School of Mathematical Sciences, North Terrace Campus, The University of Adelaide,
SA 5005 Australia*

^c*Department of Mathematics and Statistics, University of Otago, P.O. Box 56, Dunedin
9054, New Zealand*

^d*Institut des sciences de la mer de Rimouski, 310 alle des Ursulines, C.P. 3300,
Rimouski G5L 3A1 Québec, Canada*

^e*Bjerknes Center for Climate Research, Bergen, Norway*

Abstract

The theoretical foundation of a wave-ice interaction model is reported in Part 1 of this study. The model incorporates attenuation of ocean surface waves by sea ice floes and the concomitant breaking of the floes by waves that determines the structure of the marginal ice zone (MIZ). A numerical implementation of the method is presented here. Convergence of the numerical method is demonstrated, as temporal and spatial grids are refined. A semi-analytical method, which does not require time-stepping, is also developed to validate the numerical results, when dispersion is neglected. The wave energy lost during ice breakage is parameterized, as part of the numerical method. Sensitivity studies are conducted in relation to the energy loss and also dispersive effects, the choice of the attenuation model, the properties of the wave field, and sea ice properties such as concentration, thickness and breaking strain. Example simulations intended to represent conditions in the Fram Strait in 2007, which exploit reanalyzed wave and ice model data, are shown to conclude the results section. These are compared to estimates of MIZ widths based on a concentration criteria, and obtained from remotely-sensed passive microwave images.

1. Introduction

Predictions of wave and ice conditions in the marginal ice zone (MIZ) are becoming increasingly important in the era of climate change and enhanced access to the Arctic Ocean. However, contemporary sea ice models do not contain information on floe sizes, and contemporary wave models generally do not extend into the ice-covered ocean. Modeling the interactions of ocean surface waves with sea ice is necessary to rectify these conspicuous omissions, because (i) floe sizes in the MIZ are far smaller than those in the ice interior due to wave-induced ice breakage (Toyota et al., 2006), and (ii) the presence of the ice-cover strongly attenuates the waves (Wadhams et al., 1988), acting as a low-pass filter, and hence is a necessary additional consideration when modeling the transport of wave energy in the MIZ.

Part 1 of this investigation (Williams et al., submitted) describes a waves-in-ice model (WIM) that extends the work of Dumont et al. (2011) (hereafter referred to as DKB). The WIM provides predictions of (i) the ice floe size distribution (FSD) resulting from wave-induced flexural breakage of the ice cover, and (ii) the wave spectrum within the ice cover. The model includes two interrelated sub-components. First, a wave attenuation model that calculates the proportion of wave energy that is reflected by floe edges, and lost to dissipative processes, as a function of the number of ice floes encountered along the propagation path. And second, an ice breakage model that decides when the strain imposed by the passing waves on the ice cover is sufficient to cause fracture and how the resulting FSD evolves.

The FSD provided by the WIM will allow floe-size-dependent processes to be modeled in the MIZ. The smaller floe sizes in the MIZ are potentially important for thermodynamic exchanges such as lateral melting between the atmosphere, ice and ocean; dynamic exchanges, e.g. form and skin drag coefficients; and rheology, i.e. how horizontal stresses relate to deformation rates. Floe-size-dependent thermodynamic and dynamic models have been developed (e.g. Shen et al., 1986; Steele et al., 1989; Feltham, 2005), but can only be tested in fully coupled models once a floe size parameter is incorporated in sea ice models.

Email addresses: `timothy.williams@nersc.no` (Timothy D. Williams),
`luke.bennetts@adelaide.edu.au` (Luke G. Bennetts), `vernon.squire@otago.ac.nz`
(Vernon A. Squire), `dany_dumont@uqar.ca` (Dany Dumont),
`laurent.bertino@nersc.no` (Laurent Bertino)

In this paper, we place the model theory of Part 1 into a discrete spatial and temporal framework for the purpose of numerical calculations. As part of the numerical scheme, we propose a method to simulate the wave energy lost during ice breakage. Semi-analytical schemes are devised for two limiting cases of wave energy loss. These two schemes neglect dispersion, which is shown to have a negligible affect on the FSD.

Here, we consider one-dimensional transects of the ocean surface only, although the full numerical algorithm can be generalized to two-dimensional ocean surfaces. The one-dimensional restriction, however, provides a convenient setting to test the sensitivities of the WIM to the key numerical and physical parameters. Idealized incident wave and ice conditions are used to investigate the influence of the grid size, time step, the wave damping parameter, wave energy lost during ice breakage and breaking strain on the FSD produced by the WIM. Numerical experiments are also conducted with ‘realistic’ input data that represent the Fram Strait in 2007. In the absence of measured FSD data to validate the WIM, we compare our MIZ width predictions, i.e. the length of the interval of ice cover broken by waves, with MIZ widths based on a concentration criteria, using AMSR-E satellite data.

2. Statement of the problem

We consider a one-dimensional transect $x \in [0, X_2]$ of spatially varying ice concentration $c(x)$ and thickness $h(x)$. We typically use $X_2 = 450$ km. The transect is discretized into N_x grid cells with uniform widths $\Delta x = X_2/N_x$. The ice edge is located at $x = X_1$ such that the open water region is $[0, X_1]$ and the ice-covered region is $[X_1, X_2]$ (see Fig. 1). In our idealized simulations, we use an exponential thickness profile of the form

$$h(x) = \begin{cases} 0 & \text{for } 0 < x < X_1, \\ h_\infty (0.1 + 0.9 (1 - e^{-(x-X_1)/X_h})) & \text{for } X_1 < x < X_2, \end{cases} \quad (1a)$$

and a uniform concentration

$$c(x) = \begin{cases} 0 & \text{for } 0 < x < X_1, \\ c_\infty & \text{for } X_1 < x < X_2. \end{cases} \quad (1b)$$

For realistic simulations, the concentration and thickness profiles are taken from the TOPAZ operational forecasting system (Sakov et al., 2012). The

parameter X_h in (1a) was chosen to be 60 km to approximate TOPAZ thickness outputs. Table 1 lists the default values of all parameter values that are used in our simulations.

The wave energy is described by the spectral density function $S(\omega; x, t)$, where $\omega = 2\pi/T$ is the angular frequency and T is the wave period. The wave spectrum is defined in both the open ocean and the ice-covered ocean, after having undergone some attenuation. The incident wave spectrum is prescribed at $x = 0$. Because data obtained from operational wave models are usually given parametrically in terms of the significant wave height H_s and the peak period T_p (Ochi, 1998; WMO, 1998), we use the Bretschneider two-parameter spectrum (Bretschneider, 1959), i.e.

$$S(\omega; 0, t) = S_B(\omega; T_p, H_s) = \frac{1.25 H_s^2 T_p^5}{8\pi T_p^4} e^{-1.25(T/T_p)^4}. \quad (2)$$

Note that in the realistic experiments H_s and T_p evolve in time causing the incident wave spectrum to be temporally dependent. It may be possible to obtain more detailed incident wave spectra in the future—for example spectra with a parameterization of swell as well as wind waves, or the full frequency and directional spectrum.

The FSD is characterized by two spatially varying floe length parameters $D_{\max}(x, t)$ and $\langle D \rangle(x, t)$, the maximum floe length and average floe length, respectively, which also evolve with time. The detailed parameterization of the FSD is presented in §4.1 of Part 1.

3. Theoretical preliminaries

In this section we recap key definitions and ideas from Part 1.

3.1. Wave statistics

Let the displacement of the (horizontal) air-ice interface be $\eta_{\text{ice}}(x, t)$. Assuming the ice can be represented by a thin plate model, the horizontal strain in the plane of the wave is

$$\varepsilon = \frac{h}{2} \partial_x^2 \eta_{\text{ice}}, \quad (3)$$

where h is the ice thickness. The main statistics we are interested in are the mean square values of these quantities, $\langle \eta_{\text{ice}}^2 \rangle$ and $\langle \varepsilon^2 \rangle$. These give us the significant wave height H_s and the significant strain E_s :

$$H_s = 4\langle \eta_{\text{ice}}^2 \rangle^{1/2}, \quad E_s = 2\langle \varepsilon^2 \rangle^{1/2}. \quad (4)$$

The dominant wave period T_W also plays a role as, if breaking occurs, the dominant wavelength $\lambda_W = 2\pi/k_{\text{ice}}(2\pi/T_W)$ determines the maximum lengths of the consequent broken floes and it, along with $\langle \eta_{\text{ice}}^2 \rangle$ and $\langle \varepsilon^2 \rangle$, are defined in terms of integrals involving the wave spectrum S .

As discussed in Appendix A of Part 1, we assume the displacement due to a wave with the single frequency ω follows a sinusoidal profile

$$\eta_{\text{ice}}(x, t) = \text{Re}[A_{\text{ice}} e^{i(\kappa x - \omega t)}], \quad (5)$$

where κ satisfies the dispersion relation for ice-covered water, as follows

$$(F\kappa^4 + \rho(g - d\omega^2) - i\omega\Gamma)\kappa = \rho\omega^2. \quad (6)$$

In (6) F is the flexural rigidity of the ice, ρ_{ice} is the ice density, h is the ice thickness, Γ is the damping coefficient and P is the water pressure. The parameter Γ contributes to a drag pressure ($-\Gamma\partial_t\eta_{\text{ice}}$) that is proportional to the particle velocity and which is usually absent from the thin plate formulation. The rigidity is given by $F = Y^*h^3/12(1 - \nu^2)$, where Y^* is the effective Young's Modulus and $\nu = 0.3$ is the Poisson's ratio.

Let $\kappa(\omega) = k_{\text{ice}}(\omega)$ be the real positive root of (6) when $\Gamma = 0$. When $\Gamma > 0$, this root becomes complex, and $\kappa \approx k_{\text{ice}}(\omega) + i\delta(\omega)$, where $\delta > 0$ is small enough to be ignored on small-scale computations, and only makes a significant contribution to large scale wave attenuation. Also let

$$W(\omega) = \frac{gk_{\text{ice}}}{\omega^2}|\mathcal{T}|, \quad E(\omega) = \frac{h}{2}k_{\text{ice}}^2 W(\omega); \quad (7)$$

W is a factor that approximately converts the wave amplitude in open water, A , to the wave amplitude in ice, i.e. $A_{\text{ice}} \approx WA$, and \mathcal{T} is the transmission coefficient for a wave traveling from a region of open water into an ice-covered region (Williams and Porter, 2009), which depends on both ω and the ice properties involved in (6). Similarly the strain amplitude is $E_W \approx EA$.

We now define the following integrals over frequency:

$$m_n[\eta_{\text{ice}}] = \int_0^\infty S(\omega)\omega^n W^2(\omega)d\omega, \quad (8a)$$

$$m_n[\varepsilon] = \int_0^\infty S(\omega)\omega^n E^2(\omega)d\omega. \quad (8b)$$

These integrals can then be used to determine the expected response to a given wave field in a way that allows for the possibility of constructive and destructive interference between frequencies. Our main quantities of interest are then given by

$$\langle \eta_{\text{ice}}^2 \rangle = m_0[\eta_{\text{ice}}], \quad \langle \varepsilon^2 \rangle = m_0[\varepsilon], \quad T_W = 2\pi \sqrt{\frac{m_0[\eta_{\text{ice}}]}{m_2[\eta_{\text{ice}}]}}. \quad (9)$$

117 The probability of the strain amplitude exceeding the breaking strain ε_c
 118 is

$$\mathbb{P}_\varepsilon \equiv \mathbb{P}(E_W > \varepsilon_c) = \exp\left(\frac{-\varepsilon_c}{2\langle \varepsilon^2 \rangle}\right). \quad (10)$$

119 3.2. Breaking criterion

120 To determine whether the ice will be broken by waves, we define a critical
 121 probability threshold \mathbb{P}_c such that if $\mathbb{P}_\varepsilon > \mathbb{P}_c$ the ice will break. If it breaks,
 122 the maximum floe size is set to $D_{\text{max}} = \max(\lambda_W/2, D_{\text{min}})$ where D_{min} is
 123 the size below which waves are not significantly attenuated and is set to
 124 20m (Kohout and Meylan, 2008). These two quantities, D_{min} and D_{max} ,
 125 determine the FSD (see §4.1 of Part 1).

126 From (10), the criterion $\mathbb{P}_\varepsilon > \mathbb{P}_c$ can be written in terms of E_s , ε_c and \mathbb{P}_c
 127 as

$$E_s > E_c = \varepsilon_c \sqrt{-2/\log(\mathbb{P}_c)}. \quad (11)$$

128 Thus the single parameter E_c combines the effects of both ε_c and \mathbb{P}_c . Con-
 129 sequently, testing the sensitivity of the WIM to E_c allows for the combined
 130 effects of our choice of \mathbb{P}_c and also of uncertainties in the breaking strain ε_c ,
 131 which are considerable. Note that if $\mathbb{P}_c = e^{-1} \approx 0.37$, the breaking criterion
 132 becomes $E_s > \varepsilon_c \sqrt{2}$, which is the same as for a monochromatic wave.

133 3.3. Floe size distribution

134 Following DKB and Toyota et al. (2011), we use a fractal breaking model
 135 that predicts the FSD from D_{max} , D_{min} . We assume floes that break produce
 136 ξ^2 pieces, and that the fragility of the floes (the probability that a floe will
 137 break) is fixed at Π . We use $\xi = 2$ and $\Pi = 0.9$.

We determine the mean floe size from the formula of DKB:

$$\langle D \rangle = \frac{\sum_{m=1}^M (\xi \Pi)^m}{\sum_{m=1}^M (\xi^2 \Pi)^m}, \quad M = \lfloor \log_\xi(D_{\text{max}}/D_{\text{min}}) \rfloor, \quad (12)$$

138 where $\lfloor \cdot \rfloor$ denotes rounding down to the nearest integer. The FSD is discussed
 139 in more detail in §4.1 of Part 1.

140 4. Wave energy transport in the MIZ

141 4.1. Continuous equations

142 The energy balance equation for waves in the ice-covered ocean is

$$\frac{1}{c_g} D_t S(\omega; x, t) = R_{\text{in}} - R_{\text{ice}} - R_{\text{other}} - R_{\text{nl}}, \quad (13)$$

143 (Masson and LeBlond, 1989; Meylan and Masson, 2006; Ardhuin et al., 2010),
 144 where c_g is the group velocity and $D_t \equiv (\partial_t + c_g \partial_x)$. The source terms
 145 R_{in} , R_{ice} and R_{other} represent, respectively, the wind energy input, rates of
 146 energy loss to (or due to) the sea ice and the total of all other dissipation
 147 sources (e.g. friction at the bottom of the sea, losses from wave breaking or
 148 white-capping, Ardhuin et al., 2010). These are all quasi-linear in S . The
 149 R_{nl} term incorporates fully non-linear energy exchanges between frequencies
 150 (Hasselmann, 1962, 1963).

151 In the present study we consider only wave attenuation caused by the
 152 presence of ice cover. Our simplified equation is therefore

$$\frac{1}{c_g} D_t S(\omega; x, t) = -R_{\text{ice}} \approx -\hat{\alpha}(\omega, x, t) S(\omega; x, t), \quad (14)$$

153 where $\hat{\alpha}$ is the dimensional attenuation coefficient, i.e. the rate of exponential
 154 attenuation per meter. We model the wave attenuation as being the sum of
 155 linear wave scattering at floe edges and a viscosity term; this is discussed in
 156 detail in §4.2 of Part 1. The attenuation coefficient is not explicitly dependent
 157 on S , but changes suddenly when the wave energy (or more specifically the
 158 significant strain E_s) becomes large enough to cause ice breakage. This added
 159 subtlety is unique to our model and its predecessor DKB.

160 As discussed in §3.1 of Part 1, equation (14) represents advection of S at
 161 the group velocity c_g followed by its attenuation using $\hat{\alpha}$. This can be seen by
 162 considering the above problem, between breaking events, in the Lagrangian
 163 frame. The resulting expressions are

$$\frac{dx}{dt} = c_g(\omega, x, t_*) \quad \text{and} \quad (15a)$$

$$\frac{d}{dx} S(\omega; x, t) = -\hat{\alpha}(\omega; x, t_*, S_*) S(\omega; x, t), \quad (15b)$$

164 where t_* is the last time breaking occurred at x , and $S_*(\omega, x) = S(\omega; x, t_*)$.
 165 Thus, we have separated the problem into an advection problem (in which we
 166 solve $D_t S = 0$) and an attenuation one. In our numerical scheme presented
 167 in the next section, we solve (14) by alternately advecting and attenuating.

168 *4.2. Full numerical implementation*

169 Let us discretize our space, time and frequency variables using

$$\begin{aligned} \text{space:} \quad & x_j = j\Delta x & (j = 0, 1, \dots, N_x), \\ \text{time:} \quad & t_n = n\Delta t & (n = 0, 1, \dots, N_t), \\ \text{frequency:} \quad & \omega_r = \omega_0 + r\Delta\omega & (r = 0, 1, \dots, N_\omega). \end{aligned}$$

170 We choose ω_0 and $\Delta\omega$ so that 31 periods between 2.5s and 25s are included.
 171 For all temporal indices n , spatial indices j and frequency indices r , we use the
 172 shorthand notations $c_j = c(x_j)$, $h_j = h(x_j)$, $c_{g,r} = c_g(\omega_r)$, $S_{j,r}^n = S(\omega_r, x_j, t_n)$,
 173 $D_j^n = D_{\max}(x_j, t_n)$ and $\langle D_j^n \rangle = \langle D \rangle(x_j, t_n)$. The Courant number is $\mathcal{C}_r \equiv$
 174 $c_{g,r}\Delta t/\Delta x \in (0, 1]$ (for $r = 0, 1, \dots, N_\omega$). It represents the proportion of one
 175 grid cell a wave of a given frequency travels in one time step.

For $j = 1, \dots, N_x$, we also let

$$W_{j,r} = W(\omega_r), \quad E_{j,r} = E(\omega_r), \quad (16)$$

176 observing that we will need these to approximate the integrals (8). Note that
 177 W and E have an implicit dependence on the ice properties, which is why
 178 $W_{j,r}$ and $E_{j,r}$ depend on the index of the grid cell as well as the frequency
 179 index.

180 Following DKB, our numerical implementation (which we call N1) pro-
 181 ceeds as follows.

182 **1. Initialization.** For $r = 0, 1, \dots, N_\omega$:

183 We initialise the problem by setting the incident wave spectrum and
 184 initial FSD to:

$$S_{j,r}^0 = \begin{cases} S_B(\omega_r; T_p, H_s) & \text{for } j = 0, 1, 2, \\ 0 & \text{for } j = 3, 4, \dots, N_x, \end{cases} \quad (17a)$$

$$\text{and } D_j^0 = \langle D_j^0 \rangle = \begin{cases} D_{\text{init}} & \text{if } c_j > 0, \\ 0 & \text{if } c_j = 0. \end{cases} \quad (17b)$$

185 Here D_{init} is an arbitrarily chosen (relatively large) value. By invoking
 186 (17a) at $j = 0, 1, 2$, we can apply (2) via the Neumann condition
 187 $\partial_x S(\omega, 0, t) = 0$ during the advection step. Note that this implies
 188 $\partial_t S(\omega, 0, t) = 0$, since the advection equation is $D_t S = 0$. We need
 189 three points initially constant, as we advect S using a second order
 190 method.

191 **2. Time integration.** For $n = 1, 2, \dots, N_t$:
 192 For $r = 0, 1, \dots, N_\omega$:
 193 i. **Advection.** In our integration we alternate between advection
 194 and attenuation. The advection is done by solving the equation
 195 $D_t S = 0$ using the Lax-Wendroff scheme (a second order direct
 196 space-time method) with Superbee flux limiting (Roe, 1986) and a
 197 Neumann boundary condition, as mentioned above. The scheme is
 198 stable for Courant number $\mathcal{C}_r \in (0, 1]$ and has very little numerical
 199 diffusion for $0.1 \lesssim \mathcal{C}_r < 1$. We perform the advection over the
 200 whole domain in one step, mapping $S_{j,r}^{n-1}$ onto an unattenuated
 201 intermediate spectrum $\hat{S}_{j,r}^n$ ($\forall j = 1, 2, \dots, N_x$).

202 For $j = 1, 2, \dots, N_x$:
 203 We now do attenuation and the subsequent integration over fre-
 204 quency locally, i.e. we consider each cell separately. We reset
 205 $m_0[\eta_{\text{ice}}] = m_2[\eta_{\text{ice}}] = m_0[\varepsilon] = 0$, and these integrals are calcu-
 206 lated cumulatively as we loop through the frequencies.

207 For $r = 0, 1, \dots, N_\omega$:
 208 ii. **Attenuation.** We calculate the attenuation coefficient
 209 and the attenuated wave spectrum to be

$$\hat{\alpha}_{j,r}^n = \frac{\alpha_{j,r} \mathcal{C}_j}{\langle D_j^{n-1} \rangle} \quad \text{and} \quad (18a)$$

$$S_{j,r}^n = \hat{S}_{j,r}^n \exp(-\hat{\alpha}_{j,r}^{n-1} c_{g,r} \Delta t), \quad (18b)$$

210 where $\alpha_{j,r} = \alpha(x_j, \omega_r)$ is the non-dimensional attenuation co-
 211 efficient (cf. §3.1 of Part 1).

212
 213 iii. **Integration over frequency.** The integrals over fre-
 214 quency are approximated using Simpson's rule, i.e.

$$\int_0^\infty f(\omega) d\omega \approx \int_{\omega_0}^{\omega_{N_\omega}} f(\omega) d\omega \approx \sum_{r=0}^{N_\omega} w_r f(\omega_r). \quad (19)$$

215 Thus we can update the integrals we need as the r loop pro-
 216 ceeds:

$$m_0[\eta_{\text{ice}}] = m_0[\eta_{\text{ice}}] + w_r S_{j,r}^n W_{j,r}^2; \quad (20a)$$

$$m_2[\eta_{\text{ice}}] = m_2[\eta_{\text{ice}}] + w_r \omega_r^2 S_{j,r}^n W_{j,r}^2; \quad (20b)$$

$$\text{and } m_0[\varepsilon] = m_0[\varepsilon] + w_r S_{j,r}^n E_{j,r}^2. \quad (20c)$$

iv. **Floe breaking.** Having completed the frequency integration, the significant strain, E_s and the dominant period T_W is obtained from (4) and (9) following §3.2 of Part 1. If $E_s > E_c = \sqrt{2}\varepsilon_c$, the ice breaks, and we reduce the maximum floe size to $D_j^n = \max\{D_{\min}, \min\{\lambda_W/2, D_j^{n-1}\}\}$, where $\lambda_W = 2\pi/k_{\text{ice}}(2\pi/T_W)$ is the wavelength corresponding to T_W and the ice properties in the cell. We then calculate the new average floe size $\langle D_j^n \rangle$ from (12).

3. **Define the MIZ.** At the end of the integration, the point x_j is defined to be inside the MIZ if the corresponding cell contains ice and if ice breakage has occurred in that cell, i.e. if $0 < D_j^{N_t} < D_{\text{init}}$ ($j = 0, 1, \dots, N_x$). The MIZ width, L_{MIZ} , is then the distance from the ice edge to the last point in the MIZ, which includes any internal polynyas. We also define D_{MIZ} as the maximum floe size in this region.

If $\mathcal{C}_r = 1$ the waves travel one grid cell every time step and hence do not experience any attenuation from any ice they break, as the broken ice is always behind them. However, if $\mathcal{C}_r < 1$, waves travel less than a grid cell per time step and must therefore pass through a proportion of this broken ice before escaping the cell. This is because we use a *well-mixed* grid cell, as opposed to a partial grid cell. The proportion of broken ice the wave must pass through in a grid cell is $1 - \mathcal{C}_r$, i.e. it increases as the Courant number \mathcal{C}_r decreases. In our numerical results we will show that the FSD is insensitive to the exact amount of broken ice the waves travel through if the maximum Courant number $\mathcal{C} = \max\{\mathcal{C}_r | r = 0, 1, \dots, N_\omega\}$ is less than approximately $\mathcal{C} \lesssim 0.7$. This represents an equilibrium between the wave field and the FSD, which will be discussed in §4.3. In addition, while the scheme depends on the initial floe size D_{init} for $\mathcal{C} \approx 1$, it does not in the limit $\mathcal{C} \rightarrow 0$, and therefore for $\mathcal{C} \lesssim 0.7$.

4.3. Semi-analytical schemes

The N1 scheme described in the previous section is a general numerical implementation of the WIM that is applicable to any ice and wave conditions. In particular, it can deal with wave dispersion (wave speed dependent on frequency), and it is generalizable to two horizontal dimensions. However, if we neglect dispersion we can derive semi-analytic methods for the $\mathcal{C} \rightarrow 1$ and the $\mathcal{C} \rightarrow 0$ limits. The purpose of doing this is two-fold: (i) to check our numerical method; and (ii) to produce a much faster algorithm to determine MIZ width, as the frequency loop is only inside a single spatial loop instead

253 of being within both spatial and temporal loops (as in the N1 algorithm).
 254 Of course, if we wish to know the wave spectrum at a particular time in the
 255 ice—for example, if we wish to know when a group of large waves will reach
 256 a certain point, dispersive effects must be considered. Notwithstanding, it
 257 will be shown in §5.1 that the predicted FSD is insensitive to the effects of
 258 wave dispersion. Finally, we note that generalizing semi-analytical methods
 259 to the two-dimensional situation is challenging and that the numerical model
 260 is necessary to overcome the added complexity of the extra dimension.

261 When we set $\mathcal{C}_r = 1$ for all r in the N1 scheme, all of the ice breakage
 262 is caused by the lead waves as they always travel through unbroken ice.
 263 The waves do not suffer additional attenuation due to floes that have been
 264 freshly broken. Accordingly, in this situation it is possible to calculate the
 265 breaking penetration, and hence the width of the MIZ, just by considering the
 266 attenuation of the lead waves (referred to hereinafter using the superscript
 267 ‘lw’). We denote the semi-analytic method that reproduces the $\mathcal{C}_r \rightarrow 1$
 268 ($r = 0, 1, \dots, N_\omega$) limiting case by A1. This method is essentially the same
 269 as that of Vaughan and Squire (2011). The wave spectrum when the lead
 270 wave is at a given position x is given explicitly by

$$S^{\text{lw}}(\omega, x) = S(\omega, 0, 0) \exp \left(- \int_0^x \hat{\alpha}(\omega, x', 0) dx' \right). \quad (21)$$

271 We can also calculate the moments for the lead wave

$$m_\varepsilon^{\text{lw}}(x) = \int_0^\infty S^{\text{lw}}(\omega, x) E^2(\omega) d\omega \quad \text{and} \quad (22a)$$

$$m_n^{\text{lw}}(x) = \int_0^\infty \omega^n S^{\text{lw}}(\omega, x) W^2(\omega) d\omega, \quad (22b)$$

272 which give us the significant strain and the dominant wave period:

$$E_s^{\text{lw}}(x) = 2\sqrt{m_\varepsilon^{\text{lw}}(x)}, \quad \text{and} \quad T_W^{\text{lw}}(x) = 2\pi \sqrt{\frac{m_0^{\text{lw}}(x)}{m_2^{\text{lw}}(x)}}.$$

273 We can then find the width of the MIZ, i.e. the distance over which the
 274 ice cover is broken, L_{MIZ} , by solving $E_s^{\text{lw}}(L_{\text{MIZ}}) = E_c$. In practice, we still
 275 discretize the problem as before to calculate the integral (21) in which $\hat{\alpha}$
 276 varies spatially, but we no longer have to consider the time dimension. The
 277 FSD is calculated as a function of x from the wavelength corresponding to
 278 $T_W^{\text{lw}}(x)$.

279 The precise A1 algorithm proceeds as follows.

280
281

1. **Initialization.** For $r = 0, 1, \dots, N_\omega$, $j = 0, 1, \dots, N_x$:

We set the incident wave spectrum and initial FSD to be

$$S_{0,r}^{\text{lw}} = S_B(\omega_r; T_p, H_s), \quad (23a)$$

$$\text{and } D_j^0 = \langle D_j^0 \rangle = \begin{cases} D_{\text{init}} & \text{if } c_j > 0, \\ 0 & \text{if } c_j = 0. \end{cases} \quad (23b)$$

282

2. **Propagation of the lead waves.** For $j = 1, 2, \dots, N_x$:

283

284

Reset the following integrals to zero: $m_0^{\text{lw}}[\eta_{\text{ice}}] = m_2^{\text{lw}}[\eta_{\text{ice}}] = m_0^{\text{lw}}[\varepsilon] = 0$.

285

286

For $r = 0, 1, \dots, N_\omega$:

287

288

i. **Advection.** The waves move from one grid cell to the next without the effects of time-stepping and the Courant number \mathcal{C} :

289

290

$$\hat{S}_{j,r}^{\text{lw}} = S_{j-1,r}^{\text{lw}}. \quad (24)$$

291

292

ii. **Attenuation.** We calculate the dimensional attenuation coefficient from the initial FSD, so breaking effects do not influence the transmission of the waves. The energy S is also reduced accordingly at this point.

293

294

$$\hat{\alpha}_{j,r} = \frac{\alpha_{j,r} c_j}{\langle D_j^0 \rangle}, \quad \text{and} \quad (25a)$$

$$S_{j,r}^{\text{lw}} = \hat{S}_{j,r}^{\text{lw}} \exp(-\hat{\alpha}_{j,r} \Delta x). \quad (25b)$$

295

296

iii. **Integration over frequency.** We update the integrals that we need

$$m_0^{\text{lw}}[\eta_{\text{ice}}] = m_0^{\text{lw}}[\eta_{\text{ice}}] + w_r S_{j,r}^{\text{lw}} W_{j,r}^2, \quad (26a)$$

$$m_2^{\text{lw}}[\eta_{\text{ice}}] = m_2^{\text{lw}}[\eta_{\text{ice}}] + w_r \omega_r^2 S_{j,r}^{\text{lw}} W_{j,r}^2, \quad (26b)$$

$$\text{and } m_0^{\text{lw}}[\varepsilon] = m_0^{\text{lw}}[\varepsilon] + w_r S_{j,r}^{\text{lw}} E_{j,r}^2. \quad (26c)$$

297

298

299

300

301

iv. **Floe breaking.** Having finished the frequency (r) loop, we can calculate E_s^{lw} and T_W^{lw} from (26). If $E_s^{\text{lw}} > E_c$ then the ice breaks, giving a maximum floe size $D_j^{\text{lw}} = \max\{D_{\text{min}}, \min\{\lambda_W^{\text{lw}}/2, D_j^0\}\}$, where λ_W^{lw} is the wavelength corresponding to T_W^{lw} and the thickness h_j . Calculate the new average floe size $\langle D_j^{\text{lw}} \rangle$.

302 **3. Define the MIZ.** When the lead waves have left the domain, i.e. after
 303 the j loop has been completed, we can define the MIZ as in the N1
 304 scheme.

305 We denote the scheme that approximates the FSD in the $\mathcal{C} \rightarrow 0$ limit by
 306 A0. It is produced by reversing the order in which we apply breaking and
 307 attenuation in the A1 scheme. More precisely, we move the attenuation loop
 308 over r (A1.2.ii) to after the breaking step (A1.2.iv) and replace (25a) with

$$\hat{\alpha}_{j,r} = \frac{\alpha_{j,r} c_j}{\langle D_j^{\text{lw}} \rangle}. \quad (27)$$

309 Under the A1 scheme, the lead waves travel through the ice relatively
 310 unhindered, leaving broken ice in their path. The energy they lose is due to
 311 viscous damping and scattering at the relatively few floe edges they meet
 312 on their way, which is inversely proportional to the initial floe size D_{init} .
 313 Under the A0 scheme, the waves at a certain point have the same energy as
 314 if they had to travel through all the broken ice they produce. Therefore, the
 315 wave spectrum inside the broken ice is the result of an equilibrium between
 316 attenuation and breaking and is more stable.

317 An issue that is related to the two limiting cases is the amount of energy
 318 lost due to ice breakage. The A1 FSD is one extreme in which no energy
 319 is lost during this process. The A0 FSD is another critical point where the
 320 result of the amount of energy being lost is the same as the attenuation
 321 loss due to propagating through any broken floes that the waves themselves
 322 produce. Note that, if even more wave energy than this is lost, the MIZ
 323 due to the lead waves will initially be much narrower than the A0 MIZ, but
 324 following waves will gradually extend it towards the A0 limit. If less than this
 325 amount is lost during ice breakage, then we will be able to tell how sensitive
 326 the FSD is to the exact amount by testing the sensitivity of the N1 results to
 327 the \mathcal{C} parameter, which moves the N1 FSD between the A1 and A0 limits.

328 **5. Results**

329 Table 1 lists the default model parameter values used in all simulations,
 330 unless otherwise specified. Attenuation model B (from Bennetts and Squire,
 331 2012) is used with the default value of the viscous damping parameter, $\Gamma =$
 332 13 Pa s m^{-1} . In the idealized simulations of §5.1–5.2 we use the thickness and
 333 concentration profiles of (1) (also see figure 1).

334 5.1. Sensitivity to the Courant number, dispersion and horizontal resolution

335 Figure 2 presents the model sensitivity of the different numerical schemes
 336 to the Courant number in the case where dispersion is neglected, i.e. $\mathcal{C}_r = \mathcal{C}$
 337 $\forall r = 0, 1, \dots, N_\omega$. Figure 2(a) shows values of D_{\max} along a transect. Results
 338 are produced by the numerical scheme N1, in which the waves travel through
 339 proportions 0, 0.01, 0.05, 0.1 and 0.3 of the ice they break (i.e. with Courant
 340 numbers $\mathcal{C} = 1, 0.99, 0.95, 0.9$ and 0.7). Results are compared to those
 341 obtained by the two semi-analytical schemes A1 and A0. N1 and A1 agree
 342 exactly when $\mathcal{C} = 1$ while N1 and A0 agree as \mathcal{C} decreases.

343 Figure 2(b) shows a snapshot in time of the significant wave height as the
 344 waves travel further into the ice. We only show results for N1 with $\mathcal{C} = 1$ and
 345 0.9 , and the semi-analytical schemes A1 and A0 in this case. We see that H_s
 346 under the A1 scheme decreases slowly and smoothly as the lead waves travel
 347 into the ice, only being attenuated by unbroken ice. In contrast, under the
 348 A0 scheme, when the lead waves must travel through all the ice that they
 349 break, the significant wave height decreases rapidly due to the broken ice,
 350 until about $x = 110$ km. This represents the end of the A0 MIZ, where the
 351 waves reach unbroken ice and H_s drops less rapidly.

352 Under the N1 scheme with $\mathcal{C} = 1$, we can see that, as expected, the
 353 lead wave (the right-most circle) tracks the A1 curve exactly. However, the
 354 following waves have heights that are several orders of magnitude smaller.
 355 Inside the A0 MIZ, H_s for these waves tracks the A0 curve, but drops below it
 356 outside this region. This is because the lead wave with this Courant number
 357 is still able to break ice outside the A0 MIZ, so the following waves are still
 358 traveling through broken ice.

359 When \mathcal{C} drops to 0.9 , the wave heights under the N1 scheme follow the
 360 A0 ones almost exactly. Only the two right-most points (black dots) drop
 361 below the A0 curve as numerical error from the advection algorithm begins
 362 to take effect. The A0 wave heights thus represent a kind of steady-state or
 363 equilibrium solution.

364 In addition to the above, the following conclusions can be inferred from
 365 the results. First, the significant wave heights predicted by the N1 scheme
 366 for all Courant numbers agree for the interval in which they share broken
 367 ice, i.e. before the edge of the MIZ under the A0 scheme. Second, D_{MIZ} is
 368 not sensitive to the Courant number for the N1 scheme, but L_{MIZ} in the
 369 A1 and A0 limits consistently differs by a factor of about 1.6. However,
 370 the MIZ width rapidly drops to the A0 value even for N1 with $\mathcal{C} = 0.9$.
 371 That is, below a certain value, L_{MIZ} is insensitive to \mathcal{C} . As we expect that a

372 significant amount of wave energy will be lost during the breaking process,
 373 this indicates little sensitivity to the precise quantity lost, explored here by
 374 varying the Courant number.

375 In figures 3(a, b) we further investigate the sensitivity of N1 to the Courant
 376 number as a proxy for energy loss. Results are shown for both the maximum
 377 floe size, D_{MIZ} , and the width of the MIZ L_{MIZ} as functions of the peak
 378 period, for a maximum ice thickness of $h_{\infty} = 4$ m. It is again evident that
 379 the results of N1 converge rapidly to those of A0, as the Courant number
 380 decreases.

381 In figures 3(c, d) we test the effect of allowing dispersion. Results are
 382 presented for maximum Courant numbers $\mathcal{C} = 1$ and 0.1. The semi-analytical
 383 A0 scheme is also shown, and both N1 curves lie almost exactly upon it.
 384 Thus D_{MIZ} and L_{MIZ} display very little sensitivity to dispersion and when it
 385 is included the results are essentially independent of \mathcal{C} . As noted in §4.3, this
 386 is an extremely useful result for computational efficiency in the later results
 387 of this paper.

388 Two key conclusions can be drawn from figures 2 and 3. First, the nu-
 389 merical scheme is not very sensitive to the energy lost during ice breakage
 390 (parameterized by the Courant number) with the current floe breaking pa-
 391 rameterization. Second, dispersion is not necessary to calculate the FSD.
 392 Consequently, it is valid to use the numerically efficient A0 scheme to test
 393 the sensitivity of the model to the ice properties (§5.2) and for the realistic
 394 simulations presented in §5.3.

395 The final numerical issue that we investigate is the spatial resolution.
 396 Figure 4 shows the convergence of the two numerical schemes as the default
 397 grid size $\Delta x = 5$ km is reduced ten-fold. The MIZ width L_{MIZ} converges a lot
 398 faster with $\mathcal{C} = 1$ than with $\mathcal{C} = 0.7$. However, the latter only overestimates
 399 L_{MIZ} by about one or two grid cells, so using $\Delta x = 5$ km will not produce
 400 significant inaccuracies. High resolution ice-ocean models generally have grid
 401 sizes of about 2–4 km, while coarser models use approximately 10–20 km. In
 402 both cases the errors should be well below the noise level as the ice edge can
 403 be incorrectly located by as much as 40 km in contemporary models.

404 5.2. Sensitivity to wave attenuation and ice properties

405 We first revisit figures 3–4 to investigate the sensitivity of MIZ width
 406 to the ice thickness. Comparing the red A0 curves in figures 3(b, d) and fig-
 407 ure 4(b), we see that L_{MIZ} for $h_{\infty} = 2, 3$ and 4 m is respectively about 15,
 408 17 and 25 km when $T_p = 6$ s, and about 48, 55 and 75 km when $T_p = 10$ s.

Thus doubling the thickness increases the MIZ width by about 1.6. Thickness observations are much more difficult to obtain than measurements of properties such as concentration, so ice models rarely assimilate thickness. As a result model predictions for thickness can be quite inaccurate. Accordingly, the high sensitivity of our results to thickness is of potential concern. Notwithstanding, the realistic simulations presented in the following section do not show such high variability with changes to thickness.

Figures 5(a, b) show the effect of varying the damping parameter Γ in attenuation model B on the width of the MIZ predicted by our WIM. As expected, without the extra damping, i.e. when $\Gamma = 0$, waves can penetrate further into the ice-covered ocean and cause more ice breakage. The change is most pronounced for large values of the incident peak period. This is because scattering dominates the attenuation rate for small to medium values of wave period. The largest sensitivity of the width of the MIZ to Γ is for the simulation with thinner ice, shown in panel (a). This is because the flexural rigidity F in (6) is proportional to h^3 , so it quickly begins to dominate Γ at larger thicknesses, reducing the damping effect (also see the discussion in Appendix A of Part 1).

We further note that the prediction of L_{MIZ} for larger values of Γ is less sensitive to changes in thickness. In these results doubling the thickness roughly halves the MIZ width when $\Gamma = 0$, but only reduces it by a factor of approximately 1.6 when $\Gamma = 13 \text{ Pa s m}^{-1}$.

Figures 5(c) shows the effect of changing the ice concentration on the width of the MIZ. Doubling the concentration, for example, doubles the number of floe edges and thus doubles the attenuation coefficient. We may, therefore, expect this to cause L_{MIZ} to change by a factor of a half. However, the drop in L_{MIZ} in going from $c_\infty = 0.25$ to $c_\infty = 0.5$ is approximately 25% rather than 50%, and in going from $c_\infty = 0.25$ to $c_\infty = 0.75$ is approximately 50%, rather than 66%. The results therefore do not behave as simply as one can anticipate for a single monochromatic wave. In reality it represents the combined action of non-linear effects arising by considering a wave spectrum and feedback between attenuation and ice breakage.

In figure 5(d), we test the sensitivity to the breaking strain parameter E_c . This parameter incorporates the effect of the absolute breaking strain ε_c , the probability threshold \mathbb{P}_c directly, and implicitly the incident significant wave height H_s . Since the Bretschneider spectrum is proportional to H_s^2 , the significant strain will be approximately proportional to H_s . Thus doubling H_s will have about the same effect as halving the breaking strain E_c .

447 Choosing $\mathbb{P}_c = 0.01$, $e^{-2} \approx 0.1$, $e^{-1} \approx 0.37$, or $e^{-2/9} \approx 0.8$ (respectively)
448 makes $\beta_\varepsilon = E_c/E_c^{(0)} = 0.47, 0.7, 1$, or 2.1 , where $E_c^{(0)} = \varepsilon_c \sqrt{2} \approx 7.05 \times 10^{-5}$
449 is our default value, which is consistent with the limit for monochromatic
450 waves (see §3.2 and §3.2.2 of Part 1). Testing values of β_ε between $1/3$ and
451 3 should cover most reasonable variations in \mathbb{P}_c , and also our uncertainties
452 in the values of ε_c and H_s . This range gives variations of about 50%. Again
453 though, when we move to more realistic tests where the different variables
454 interact in more complicated ways, there is generally a lot less variation with
455 β_ε than is observed here.

456 5.3. Realistic experiments in the Fram Strait

457 Here we repeat some of the sensitivity studies in simulations using the
458 A0 scheme with realistic wave forcings, ice concentrations and ice thicknesses
459 along a transect of the Fram Strait during 2007. Figure 6 shows a map of
460 the area and the location of the transect. It also shows the location of the
461 grid cell where wave forcing data was extracted from the WAM ERA-Interim
462 reanalysis. Figure 7(a) shows a time series of this wave forcing, while fig-
463 ures 7(b,c) show, respectively, ice concentrations and thicknesses obtained
464 from a TOPAZ reanalysis (Sakov et al., 2012) in which concentration data
465 derived from the Ocean and Sea Ice Satellite Application Facility (OSI SAF,
466 met.no) have been assimilated. On average, the modeled ice edge is 45 km
467 west of the ice edge observed by AMSR-E (University of Bremen) and de-
468 termined from the analysis of Kloster and Sandven (2011), which is plotted
469 as a solid line in 7(b). This discrepancy is well within the uncertainties and
470 resolution of the model (TOPAZ has a resolution of about 13 km) and the
471 resolution of the AMSR-E analysis. (Kloster and Sandven, 2011, the tran-
472 sect from 15°W to 5°E was divided into bins with widths of about 21.2 km,
473 i.e. 1 degree in longitude, and analyzed for ice concentration.) The internal
474 concentrations from the model and the data also compare well.

475 Also plotted (dashed line) in figure 7(b) is an estimate for the inner edge
476 of the MIZ, determined from the same AMSR-E concentrations using the
477 criterion that $c < 0.9$ corresponds to the MIZ. While this is a different
478 criterion from the floe size criterion, where we define the MIZ by whether
479 the ice is broken or not—see step 3 of the N1 algorithm in §4.2 we use in
480 this paper—it provides a rough estimate of the accuracy of the predictions
481 obtained from our WIM (Strong, 2012).

482 The mean ice thickness is roughly 0.8 m, creeping up towards 2 m in the
483 summer, which is thicker due to greater movement south of multi-year ice

484 from the Arctic Ocean at that time. According to Widell et al. (2003), these
 485 ice thicknesses are probably too low, so we have also run simulations in which
 486 the ice thicknesses are multiplied by a factor $\beta_h = 1.75$ or 2.5 in order to
 487 get closer to observations. We observe that the Fram Strait is a particularly
 488 challenging MIZ to model, as it is made up of sea ice that is continuously
 489 being channeled out of the Arctic Basin, locally-growing sea ice in winter,
 490 and liberated land fast ice that can include sikussak. It is also baroclinically
 491 unstable so its edge is often characterized by the presence of many eddies
 492 and meanders.

493 Figure 8 shows the results of numerical experiments using the model out-
 494 lined in this work. Results for the expected ice breakage are calculated daily
 495 using either the TOPAZ thicknesses or the increased thicknesses, the TOPAZ
 496 concentrations and the ERA-Interim waves. Floe sizes are re-initialized for
 497 each model pass to be uniformly $D_{\text{init}} = 500$ m long. An extension to in-
 498 clude a memory in each cell of D_{max} and a gradual refreezing was rejected
 499 on the basis that we are unable to embed the more important effects of ice
 500 movement due to winds and current into this one-dimensional experiment.

501 Figures 8(a,c) show the results when attenuation model B is used with
 502 $\Gamma = 13 \text{ Pa s m}^{-1}$. The variations are systematic in that increasing the thick-
 503 ness or breaking strain makes the MIZ narrower. For the winter months, MIZ
 504 widths estimated from our ice breakage model are about half the widths de-
 505 termined from the AMSR-E-measured concentrations. In the summer, when
 506 the wave heights are much lower and the ice is thicker, there is a lot less
 507 ice breakage, whereas the concentration criterion defines the MIZ as being
 508 much larger than the winter. This could be due to the more dilute ice being
 509 able to spread out even further in response to stresses from off-ice winds
 510 and currents. The neglected effect of ice advection would thus become more
 511 important in this period as well.

512 Figure 8(a) shows the variation of the MIZ width with thickness. There
 513 is more variation in the summer when the ice is already very thick. However,
 514 in the winter, the variations are much reduced, both in comparison with the
 515 summer variability and the idealized results of the previous section.

516 Figure 8(c) shows that the MIZ width responds to variations in the break-
 517 ing strain in a similar way that it did to thickness variations. Again, there is
 518 significantly more variation in the summer, but the winter results are much
 519 less sensitive than they would be expected to be from idealized experiments.

520 Figure 8(b) shows that the biggest source of variability comes from the
 521 choice of viscosity parameter Γ . When $\Gamma = 0$, maxima in the winter MIZ

widths (reflecting days with strong incident wave fields) often reach about 0.8–1.0 times the AMSR-E widths, but are generally about one half to one third of them. The noise in the curves reflects the day-to-day variations in the incident wave fields. In the summer, all three values of Γ predict very low widths due to the weak incident waves. With Γ increased to 6.5 Pa s m^{-1} , the values of L_{MIZ} drop and become much closer to the widths produced by using $\Gamma = 13 \text{ Pa s m}^{-1}$. This behaviour was also observed in the previous section, where results were variable with Γ when low values were used, but were more stable for Γ in the range $6.5\text{--}13 \text{ Pa s m}^{-1}$. The default value of 13 Pa s m^{-1} was chosen to make the attenuation of long waves match the measurements of Squire and Moore (1980), as they can not be fully explained by present scattering theory. While low frequency measurements can have more noise in them, and more experiments to confirm these attenuation results are necessary, the stability of our results over the correct order of magnitude is encouraging.

Our results do, however, suggest that a (modeled) floe size criterion and a concentration criterion for the MIZ may give different predictions for its boundary. It is likely that a combination of the two should be used to model the large scale deformations of the ice. This emphasizes the need for more measurements of floe sizes and large scale deformations in the MIZ to determine how the two criteria are related and how they should be used to precisely define the MIZ. It is also very likely that floe size and concentration are interlinked variables that will need to be consistently related to one another, once incorporated in a sea ice model. The above results also highlight the importance of obtaining a better understanding of the attenuation process and, in particular the lower-than-observed attenuation of long waves than is predicted by scattering theory. It also shows the urgent need for more measurements of attenuation and of more reliable thickness data.

6. Incorporating the WIM into coupled ice-ocean models

The WIM presented in this two-part paper is designed to be integrated into an ice/ocean model (IOM), such as HYCOM. Specifically, by WIM we mean the numerical scheme N1, as this is more easily generalized to two horizontal dimensions. The A0 and A1 schemes were implemented to provide checks for the N1 scheme in different limiting cases and also to provide fast results in this one-dimensional setting. However, it is much more difficult to generalize the semi-analytical schemes to two dimensions.

558 We envisage the WIM to be a separate module that is called periodically
 559 to update the floe size distribution (FSD). The wave model component of
 560 the IOM, e.g. WAM or WAVEWATCH III[®], will provide the wave forcing
 561 boundary condition required in the WIM. The sea ice model component of
 562 the IOM, e.g. CICE, will provide the ice conditions for the WIM. We note
 563 that the quantities provided by the wave and sea ice models to the WIM are
 564 likely to require interpolation onto the high resolution grid it uses. The FSD
 565 computed by the WIM will be an input parameter for a number of other
 566 parameterizations in the IOM. For example, it can be used to distinguish
 567 between the pack ice and the MIZ, and thus to decide which large-scale rhe-
 568 ology should be used to determine the ice deformation. The thermodynamic
 569 model of Steele (1992), for example, could also be applied to the FSD to
 570 allow for lateral melting (or freezing). We also note that the sub-components
 571 of the WIM (cf. §4 of Part 1) are independent and so, once the skeleton of
 572 the WIM is implemented, they can be easily updated whenever new data are
 573 obtained or new theoretical progress is made. The implementation of the
 574 WIM inside the TOPAZ operational analysis and forecasting system, which
 575 is based on the Hybrid Coordinate Ocean Model (HYCOM) and the sea ice
 576 model of Drange and Simonsen (1996), is in progress and will be the focus
 577 of a future manuscript. The sea ice model of Drange and Simonsen (1996) is
 578 similar to CICE.

579 **7. Summary and overall conclusions**

580 In Part 2 of this two-part series, we have developed the theory of wave-ice
 581 interactions, presented in Part 1, into a numerical algorithm that predicts
 582 the FSD and wave spectrum in the MIZ, given an incident wave spectrum
 583 at the ice edge, and ice thickness and surface concentration profiles. Our
 584 investigation focused on the predictions of the FSD.

585 The numerical WIM was outlined for one-dimensional transects, as a step
 586 towards the full two-dimensional model. But the restriction was also imposed
 587 to facilitate a thorough sensitivity study, with respect to the key numerical
 588 and physical parameters in the WIM. This is especially important because
 589 of the high degree of uncertainty in many of these quantities. Sensitivity
 590 studies were conducted, in the first instance, using idealized ice thickness
 591 and concentration profiles. The most substantive observations follow.

- 592 1. Sufficient convergence of the FSD is given by a spatial resolution of
 593 approximately 5 km.

- 594 2. The waves can be forced to travel through an arbitrary proportion
595 of the ice they break by adjusting the Courant number in the time
596 stepping component of the numerical algorithm. This serves as a proxy
597 for wave energy lost during ice breakage. When the waves only travel
598 through a small proportion of broken ice, small changes in the exact
599 proportion can lead to large changes in the width of the MIZ. But,
600 this sensitivity quickly reduces, and the MIZ width is unaffected by
601 the exact proportion when the waves travel through more than 30 % of
602 the broken ice.
- 603 3. Neglecting dispersion of the wave spectrum does not affect the FSD
604 predicted by the WIM. Semi-analytical models, which do not incorpo-
605 rate dispersion, were therefore proposed for the two limiting cases of
606 wave energy loss during ice breakage. The semi-analytical models are
607 numerically efficient and helped to validate the full numerical model.
608 However, it was noted that it will be difficult to generalize these models
609 to two-dimensions.
- 610 4. The FSD is highly sensitive to the values of the damping parameter Γ ,
611 the ice thickness, and the breaking strain parameter. This emphasizes
612 the need for more measurements of ice thickness, wave attenuation and
613 breaking strains, as well as *in situ* observations of ice breaking.

614 The WIM was also tested using realistic input parameters that repre-
615 sented the Fram Strait in 2007. The sensitivity of the FSD predicted by
616 the WIM to the ice thickness and breaking strain parameter was lower than
617 in the idealized simulations. However, sensitivity to Γ remained high. It is
618 therefore crucial to resolve the problem of how long waves are attenuated the-
619 oretically, and also to conduct more experiments to confirm the observations
620 of Squire and Moore (1980) and to extend them to different ice types.

621 To conclude, the MIZ widths obtained from the realistic simulations, i.e.
622 the distance of broken ice in the model, were compared to MIZ widths deter-
623 mined from contemporaneous AMSR-E (University of Bremen) concentration
624 data. In winter months, when waves are at their strongest, the MIZ widths
625 predicted by the WIM were roughly half those predicted by the concentration
626 criterion. In the summer, the model results and the concentration results give
627 quite different boundaries to the MIZ. Probably this is partly due to smaller
628 waves and thicker ice in this time period, partly to neglected effects like ice
629 advection and thermodynamic effects, and partly due to the two different
630 definitions of the MIZ. This highlights the need for more measurements of

the FSD, and also more research on how to define the MIZ (in our case, for the purpose of determining which large-scale ice rheology to use) more precisely. The model proposed in this two-part series has been motivated by the many observations that suggest a primary role for ocean waves in shaping the morphology of ice fields. Waves habitually limit the size of the constituent ice floes throughout the MIZ, by fracturing those floes that are too large to exist as the waves permeate further into the ice pack. Attenuation, arising due to scattering and supplementary inelastic processes such as turbulence, bending hysteresis and interfloe collisions and rafting, also occurs causing a gradual reduction of the wave energy envelope with distance from the ice edge that, *cæteris paribus*, results in a gradual increase in floe size with penetration. The FSD is therefore continuously modified by pervasive incident ocean wave trains that, according to their period, may either travel long fetches from distant storms or else be more locally generated. They are then preferentially filtered by the sea ice in a manner that favors the survival of longer wavelengths.

Given these several influential factors relating to the composition of MIZs, it is perhaps surprising to the reader that wave-ice interactions have not been included in ice/ocean models hitherto. While it has been discussed in the past, the complexity of doing this has proved insuperable until now. We have provided a potential way to do it, and have given some first predictions of how floe sizes and MIZ width are manipulated by waves in a one-dimensional spectral setting. Most importantly, we have established the machinery to deal with the next stage of development, which is to incorporate two-dimensional interactions arising from a directional sea comprising energy at a comb of different frequencies distributed angularly.

Acknowledgement

The work described herein is embedded within the Waves-in-Ice Forecasting for Arctic Operators (WIFAR) project, coordinated by Nansen Environmental and Remote Sensing Center (NERSC) and funded by the Research Council of Norway and Total E&P Norge through the Programme for Optimal Management of Petroleum Resources (PETROMAKS). The authors acknowledge with gratitude this funding and the support of the University of Otago, New Zealand. They thank Aleksey Marchenko for useful discussions, and Francois Counillon for discussions and assistance with regard to

666 the TOPAZ data. They also thank the anonymous reviewers of this and
667 earlier versions of this paper for extremely constructive criticisms.

668 **References**

- 669 Ardhuin, F., Rogers, E., Babanin, A. V., Filipot, J.-F. Magne, R., Roland,
670 A., van der Westhuysen, A., Queffelec, P., Lefevre, J.-M., Aouf, L., Col-
671 lard, F., 2010. Semiempirical dissipation source functions for ocean waves.
672 Part I: Definition, calibration, and validation. *J. Phys. Oceanogr.* 40, 1917–
673 1941.
- 674 Bennetts, L. G., Squire, V. A., 2012. On the calculation of an attenua-
675 tion coefficient for transects of ice-covered ocean. *Proc. R. Soc. Lond. A*
676 468 (2137), 136–162.
- 677 Bretschneider, C. L., 1959. Wave variability and wave spectra for wind-
678 generated gravity waves. Tech. Mem. 118, Beach Erosion Board, U.S. Army
679 Corps Eng.
- 680 Drange, H., Simonsen, K., 1996. Formulation of air-sea fluxes in the ESOP2
681 version of MICOM. Tech. Rep. 125, Nansen Environmental and Remote
682 Sensing Center, Thormøhlensgate 47, Bergen 5006, Norway.
- 683 Dumont, D., Kohout, A. L., Bertino, L., 2011. A wave-based model for the
684 marginal ice zone including a floe breaking parameterization. *J. Geophys.*
685 *Res.* 116 (C4), 1–12.
- 686 Feltham, D. L., 2005. Granular flow in the marginal ice zone. *Phil. Trans. R.*
687 *Soc. Lond. A.* 363, 1677–1700.
- 688 Hasselmann, K., 1962. On the non-linear transfer in a gravity-wave spectrum.
689 Part 1. General Theory. *J. Fluid Mech.* 12, 481–500.
- 690 Hasselmann, K., 1963. On the non-linear transfer in a gravity-wave spectrum.
691 Part 3. Computation of the energy flux and swell-sea interaction for a
692 Neumann spectrum. *J. Fluid Mech.* 15, 385–398.
- 693 Kloster, K., Sandven, S., 2011. Ice motion and ice area flux in the Fram Strait
694 at 79N using ASAR and passive microwave for Feb. 2004 – Jul. 2010. Tech.
695 Rep. 322, Nansen Environmental and Remote Sensing Center.

- 696 Kohout, A. L., Meylan, M. H., 2008. An elastic plate model for wave at-
697 tenuation and ice floe breaking in the marginal ice zone. *J. Geophys. Res.*
698 113 (C09016), doi:10.1029/2007JC004434.
- 699 Masson, D., LeBlond, P. H., 1989. Spectral evolution of wind-generated sur-
700 face gravity waves in a dispersed ice field. *J. Fluid Mech.* 202, 111–136.
- 701 Meylan, M. H., Masson, D., 2006. A linear Boltzmann equation to model
702 wave scattering in the marginal ice zone. *Ocean Modelling* 11 (3-4), 417–
703 427.
- 704 Ochi, M. K., 1998. *Ocean waves. A Stochastic approach.* Cambridge Univer-
705 sity Press.
- 706 Roe, P. L., 1986. Characteristic-based schemes for the euler equations. *Annu.*
707 *Rev. Fluid Mech.* 18, 337–365.
- 708 Sakov, P., Counillon, F., Bertino, L., Lisæter, K. A., Oke, P. R., Korablev,
709 A., 2012. TOPAZ4: an ocean-sea ice data assimilation system for the North
710 Atlantic and Arctic. *Ocean Science* 8, 633–656.
- 711 Shen, H. H., Hibler, W. D., Leppäranta, M., 1986. On applying granular flow
712 theory to a deforming broken ice field. *Acta Mechanica* 63, 143–160.
- 713 Squire, V., Moore, S. C., 1980. Direct measurement of the attenuation of
714 ocean waves by pack ice. *Nature* 283 (5745), 365–368.
- 715 Steele, M., 1992. Sea ice melting and floe geometry in a simple ice-ocean
716 model. *J. Geophys. Res.* 97 (C11), 17729–17738.
- 717 Steele, M., Morison, J. H., Untersteiner, N., 1989. The partition of air-ice-
718 ocean momentum exchange as a function of ice concentration, floe size,
719 and draft. *J. Geophys. Res.* 94 (C9), 12739–12750.
- 720 Strong, C., 2012. Atmospheric influence on Arctic marginal ice zone position
721 and width in the Atlantic sector, February-April 1979-2010. *Clim. Dyn.*
722 39 (12), 3091–3102.
- 723 Toyota, T., Haas, C., Tamura, T., 2011. Size distribution and shape proper-
724 ties of relatively small sea-ice floes in the Antarctic marginal ice zone in
725 late winter. *Deep-Sea Res. II* 58 (9–10), 1182–1193.

- 726 Toyota, T., Takatsuji, S., Nakayama, M., 2006. Characteristics of sea ice floe
727 size distribution in the seasonal ice zone. *Geophys. Res. Lett.* 33 (L02616).
- 728 Vaughan, G. L., Squire, V. A., 2011. Wave induced fracture probabilities for
729 arctic sea-ice. *Cold Regions Sci. Tech.* 67 (1–2), 31–36.
- 730 Wadhams, P., Squire, V. A., Goodman, D. J., Cowan, A. M., Moore, S. C.,
731 1988. The attenuation rates of ocean waves in the marginal ice zone. *J.*
732 *Geophys. Res.* 93 (C6), 6799–6818.
- 733 Widell, K., Østerhus, S., Gammelsrød, T., 2003. Sea ice velocity in the
734 Fram Strait monitored by moored instruments. *Geophys. Res. Lett.*
735 30 (L018119).
- 736 Williams, T. D., Bennetts, L. G., Squire, V. A., Dumont, D., Bertino, L.,
737 submitted. Wave-ice interactions in the marginal ice zone. Part 1: Theo-
738 retical foundations. *Ocean Modelling*.
- 739 Williams, T. D., Porter, R., 2009. The effect of submergence on the scattering
740 by the interface between two semi-infinite sheets. *Journal of Fluids and*
741 *Structures* 25, 777–793.
- 742 World Meteorological Organization, 1998. Guide to Wave Forecasting and
743 Analysis, 2nd Edition. WMO No. 702. World Meteorological Organization.

Table 1: Default model parameters.

Quantity	Symbol	Value
Ice thickness	h_∞	1–4 m
Ice concentration	c_∞	0.75
Water density	ρ	1025 kg m^{-3}
Ice density	ρ_{ice}	922.5 kg m^{-3}
Gravitational acceleration	g	9.81 m s^{-2}
Brine volume fraction	v_b	0.1
Incident significant wave height	H_s	3 m
Incident peak period	T_p	6–10 s
Minimum floe size in FSD	D_{min}	20 m
FSD cut-off length	D_{unif}	200 m
Initial value of D_{max}	D_{init}	500 m
Fragility	Π	0.9
Number of broken pieces	ξ	2
Number of spatial grid cells	N_x	91
Grid size	Δx	5 km
Time step	Δt	400 s
Number of spectral components	N_ω	31
Minimum wave period	$T_{30} = 2\pi/\omega_{30}$	2.5 s
Maximum wave period	$T_0 = 2\pi/\omega_0$	23.8 s
Spectral resolution	$\Delta\omega$	$7.5 \times 10^{-2} \text{ s}^{-1}$
Breaking probability threshold	\mathbb{P}_c	$e^{-1} \approx 0.37$
Flexural strength	σ_c	0.27 GPa
Effective Young’s modulus	Y^*	5.5 GPa
Breaking strain	ε_c	4.99×10^{-5}
Breaking significant strain	$E_c = \varepsilon_c \sqrt{2}$	7.05×10^{-5}
Viscous damping parameter	Γ	13.0 Pa s m^{-1}

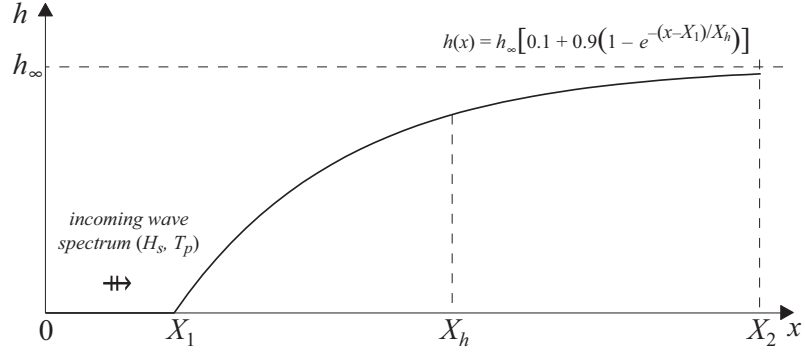


Figure 1: Schematic figure illustrating the ice thickness profile in relation to the incident wave field. We generally assume the latter is prescribed at $x = 0$ using a Bretschneider spectrum of the form (2), parameterized in terms of the significant wave height H_s and peak period T_p . The thickness and concentration are either given by (1) or are taken from TOPAZ model outputs.

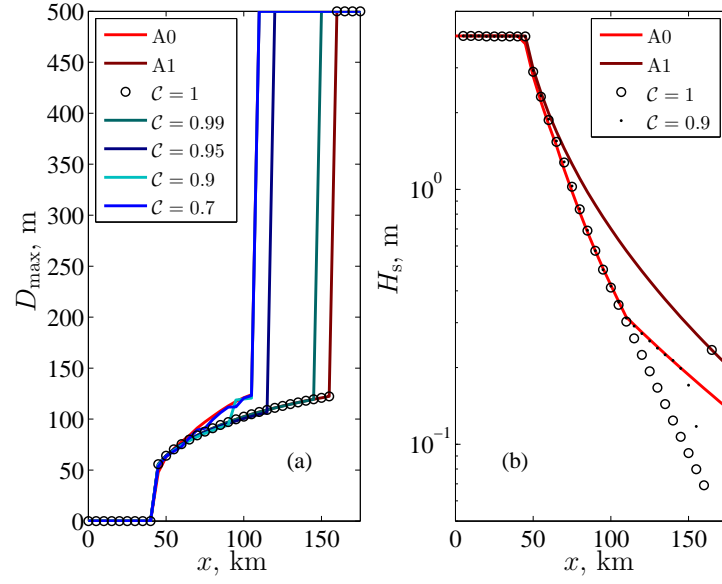


Figure 2: General properties of the WIMs. Dispersion is neglected, the incident wave spectrum has $T_p = 9.5$ s, and the ice thickness used in (1a) is $h_\infty = 4$ m. (a): Values of D_{\max} after using the A0 and A1 semi-analytic schemes, or the N1 scheme with the indicated values of \mathcal{C} . (b): Significant wave height at time $t = 2.02$ h.

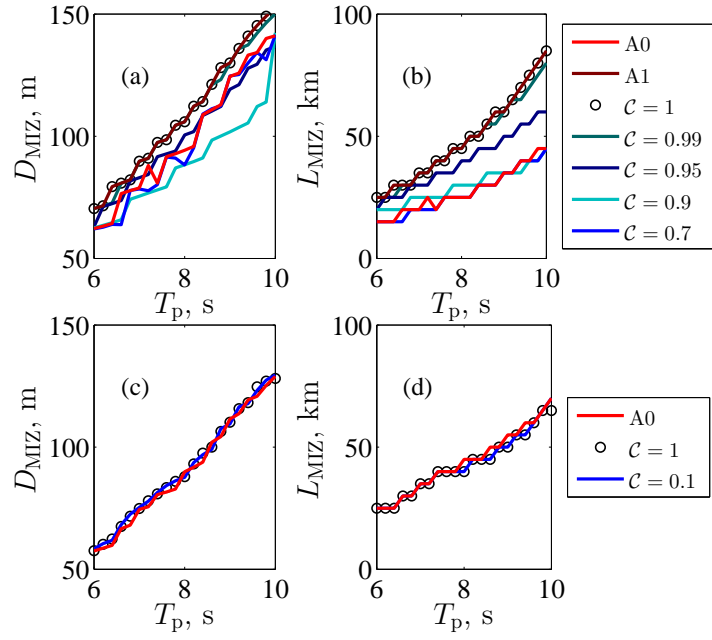


Figure 3: Behaviour of numerical scheme N1 with maximum CFL number, \mathcal{C} , and comparison with the A0 and A1 semi-analytic schemes. (a, b): Dispersion is neglected. The ice thickness used comes from equation (1a) with $h_\infty = 4$ m. (c, d): Dispersion is included. The ice thickness used is $h_\infty = 2$ m.

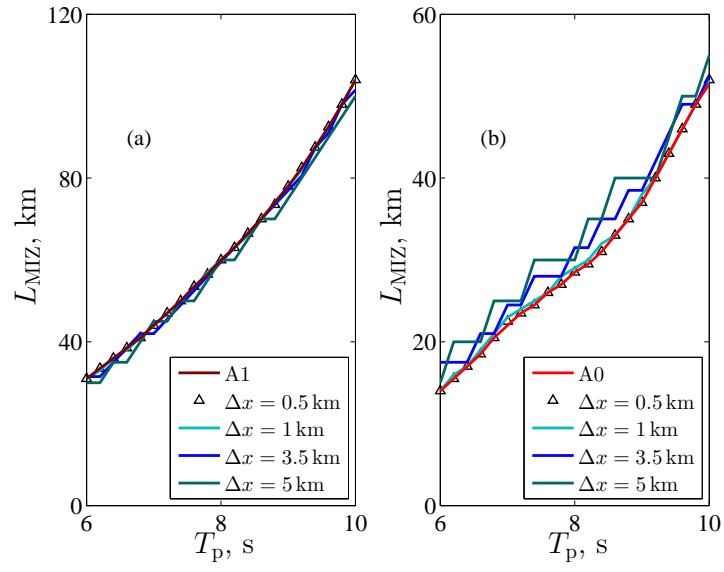


Figure 4: Behaviour of numerical schemes with grid size, Δx . (a): Value of L_{MIZ} after using scheme A1 ($\Delta x = 0.5$ km), or N1 with $C = 1$ and the indicated values of Δx (b): Same as (a), but with scheme A0 instead of A1, and N1 used with $C = 0.7$ instead of 1. The ice thickness used in (1a) is $h_\infty = 3$ m.

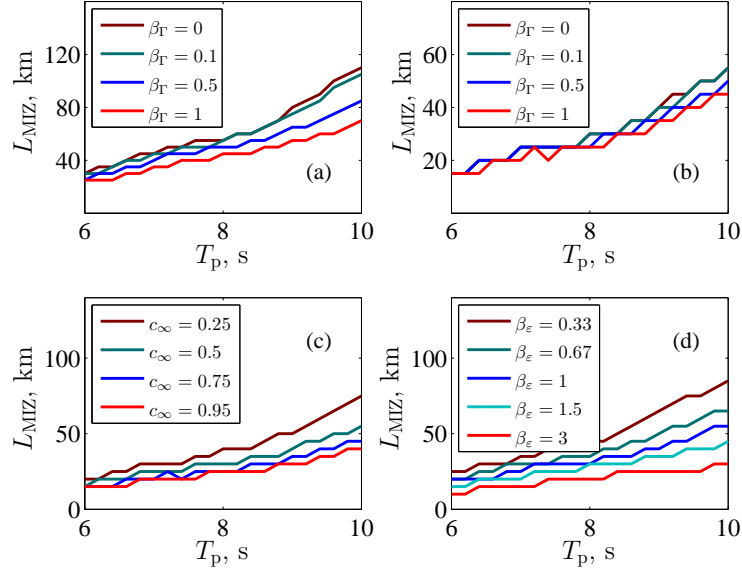


Figure 5: The effect of the attenuation model and ice concentration. (a, b): Values of L_{MIZ} after using the semi-analytic scheme A0 and attenuation model B with $\Gamma = \beta_{\Gamma} \times 13 \text{ Pa s m}^{-1}$ and the indicated value of β_{Γ} . The ice thicknesses used in (1a) are $h_{\infty} = 2 \text{ m}$ (a) and $h_{\infty} = 4 \text{ m}$ (b). (c): Values of L_{MIZ} after using the A0 scheme with the indicated values of c_{∞} used in (1b), and with $h_{\infty} = 2 \text{ m}$ in (1a). (d): The effect of the parameter E_c . Values of L_{MIZ} after using WIM A0 with $E_c = \beta_{\epsilon} \sqrt{2} \epsilon_c$, where $\epsilon_c \approx 4.99 \times 10^{-5}$ and β_{ϵ} is indicated. The ice thickness used is $h_{\infty} = 3 \text{ m}$.

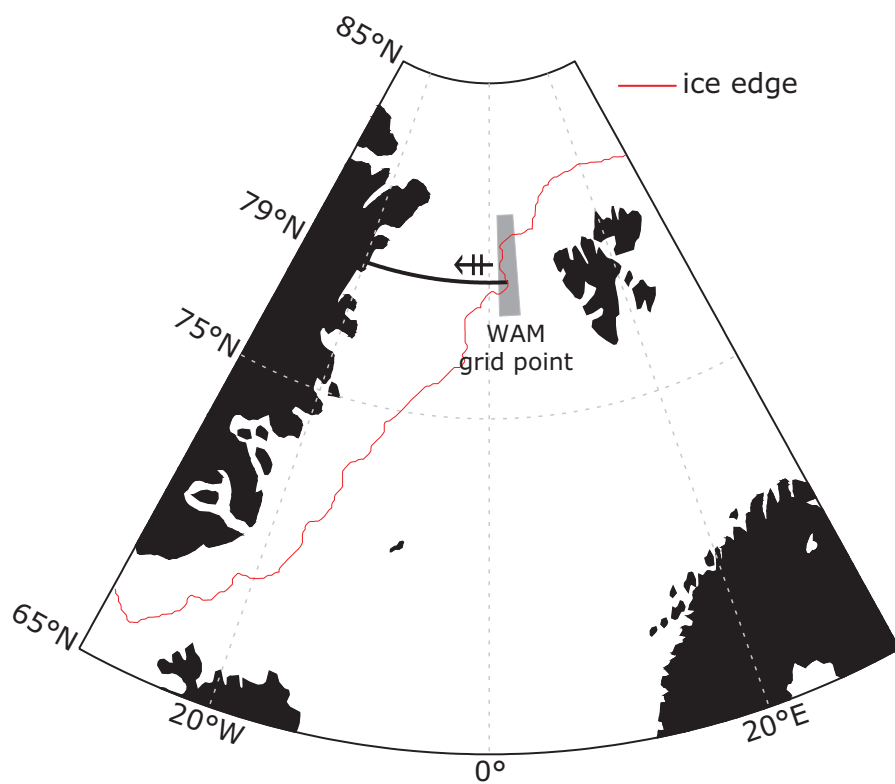


Figure 6: Map of the Fram Strait area showing the observed ice edge on 7 November 2007 (red line). The thick black line along 79N shows the location where the ice parameters were extracted for the simulations; this is where the WIM is tested. The gray box shows the grid cell from which ocean wavefields were extracted from the WAM ERA-Interim reanalysis.

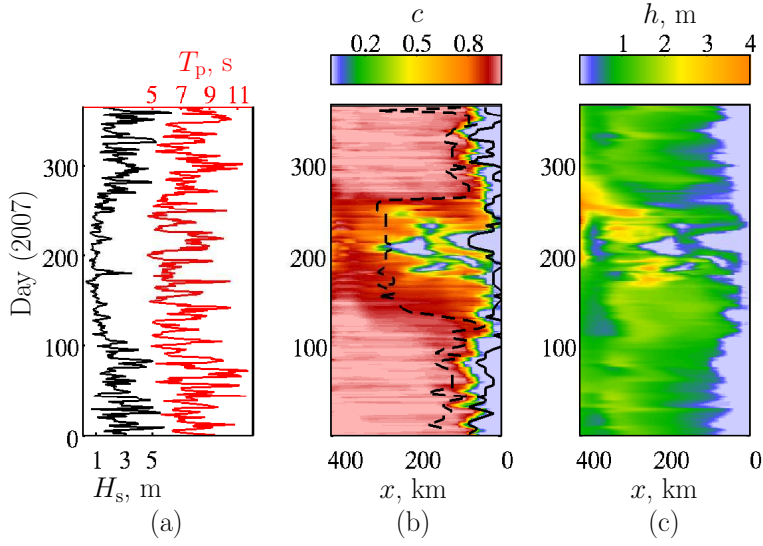


Figure 7: Model data for our one-dimensional simulations in the Fram Strait in 2007, between the south-east coast of Norske Øer (latitude 79°N , longitude 17.7°W), which corresponds to $x = 438\text{ km}$ on our one-dimensional grid, and latitude 79°N , longitude 3°E , which corresponds to $x = 0$. The wave field is specified at $x = 0$ and is obtained from the WAM ERA-Interim reanalysis. The significant wave heights and peak periods are plotted in (a). The waves are then advected west through ice with concentrations and thicknesses taken from a TOPAZ reanalysis. They are interpolated onto a regular grid with longitudinal resolution of 0.125° ($\Delta x = 2.65\text{ km}$), and are plotted in (b) and (c). For comparison, the ice edge and edge of the MIZ estimated from AMSR-E concentrations are also plotted in (b) as solid and dashed black lines respectively.

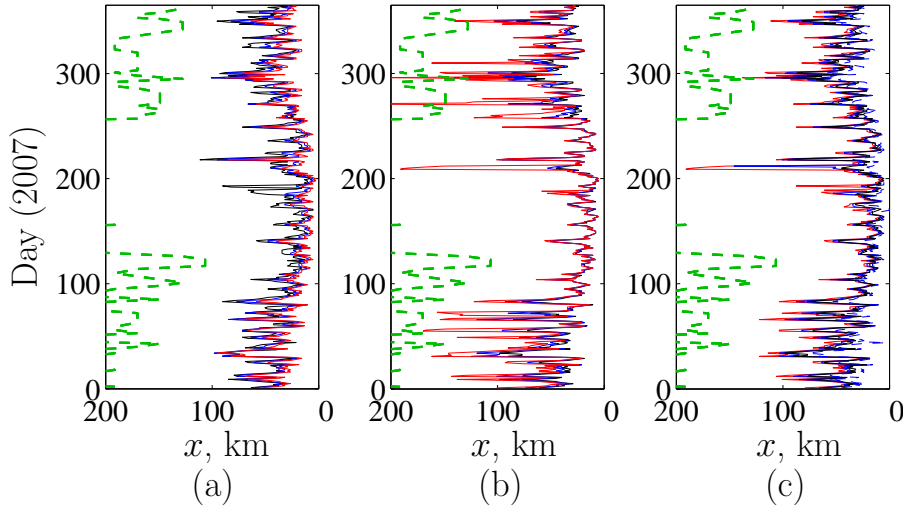


Figure 8: Results of one-dimensional simulations in the Fram Strait in 2007. (a): L_{MIZ} determined by semi-analytical scheme A0 with $\beta_h = 1$ (—), $\beta_h = 1.75$ (—) and $\beta_h = 2.5$ (—), where β_h is a factor used to increase the ice thicknesses from figure 7(c), which are unrealistically low. The breaking strain ε_c is 4.99×10^{-5} , determined from Part 1 (§4.3), using $\nu_b = 0.1$. (b): L_{MIZ} determined by WIM A0 using attenuation model B with $\beta_h = 1.75$ and $\Gamma = \beta_\Gamma \times 13 \text{ Pa s m}^{-1}$, where $\beta_\Gamma = 0$ (—), $\beta_\Gamma = 0.5$ (—) and $\beta_\Gamma = 1$ (—). (c): L_{MIZ} determined by WIM A0 using attenuation model B with $\Gamma = 10 \text{ Pa s m}^{-1}$, $\beta_h = 1.75$, and $E_c = 7.05\beta_\varepsilon \times 10^{-5}$, where $\beta_\varepsilon = 0.5$ (—), $\beta_\varepsilon = 0.75$ (—), $\beta_\varepsilon = 1$ (—) and $\beta_\varepsilon = 2$ (—). The factor β_ε is included to test the sensitivity to the breaking strain and other parameters such as the probability threshold \mathbb{P}_c and H_s . For comparison, the MIZ width estimated from AMSR-E concentrations is plotted as a dashed green line in all plots. (This is the distance between the two black lines in Figure 7(b).)